Scientific Research Publishing

Journal of Geoscience and Environment Protection, 2026, 14(8), 80-99
https://www.scirp.org/journal/gep
ISSN Online: 2327-4344
ISSN Print: 2327-4336

Resistivity Structure of the Korosi Geothermal Field, Kenya, from Three Dimensional Magnetotelluric Inversion

Claire Kimeli[1*], Justus Maithya[1], Josphat Mulwa[2], John Githiri[1], Isaac Kanda[3]

[1]Department of Physics, Jomo Kenyatta University of Agriculture and Technology, Nairobi, Kenya
[2]Department of Earth & Climate Science, University of Nairobi, Nairobi, Kenya
[3]Geothermal Development Company, Nairobi, Kenya
Email: *jelangat.claire@students.jkuat.ac.ke

How to cite this paper: Kimeli, C., Maithya, J., Mulwa, J., Githiri, J. and Kanda, I. (2026). Resistivity Structure of the Korosi Geothermal Field, Kenya, from Three Dimensional Magnetotelluric Inversion. *Journal of Geoscience and Environment Protection, 14,* 80-99.
https://doi.org/10.4236/gep.2026.148005

Received: July 21, 2026
Accepted: August 17, 2026
Published: August 20, 2026

Abstract

The Magnetotelluric (MT) method is widely used to image subsurface electrical resistivity and characterize geothermal systems at depth. In this study, 81 MT soundings were analyzed to assess the geothermal resource and map the subsurface resistivity distribution of the Korosi geothermal field within the Kenya rift. Phase tensor analysis of the impedance data showed that skew angles and ellipticity increase with period, pointing to a largely three-dimensional (3D) resistivity distribution beneath the geothermal field. Consequently, the full impedance tensor was inverted using the ModEM three-dimensional inversion code. The recovered model, examined along three west-east profiles, reveals a broadly consistent three-layer resistivity structure. It comprises a thin near surface resistive layer (>100 Ωm) interpreted as relatively dry or weakly altered volcanic rocks, an extensive conductive zone (<10 Ωm) interpreted as a hydrothermally altered clay cap and deeper resistive bodies (>100 Ωm) that may represent higher temperature alteration zones, dense intrusive rocks or low-porosity volcanic units. The conductive anomalies vary considerably in thickness and lateral continuity across the field. Western conductors extend toward the Nakaporon fault zone, whereas eastern conductors occur toward the Nagoreti area. These conductive zones are locally separated by relatively resistive domains, suggesting that hydrothermal alteration is not uniformly distributed beneath the Korosi volcanic complex. The spatial relationship between the conductive anomalies and mapped faults suggests that these structures may influence fluid circulation, alteration patterns and compartmentalization of the geothermal system.

Keywords

Korosi Geothermal Field, Magnetotelluric, 3D Inversion, Resistivity, Kenya Rift

1. Introduction

Geothermal resources originate deep within the Earth's crust and are exploited globally for electricity generation and various direct-use applications. As a clean, abundant, and reliable renewable energy source, geothermal power provides stable power generation completely independent of short-term weather fluctuations or seasonal variations (Dickson & Fanelli, 2013). Consequently, contemporary global energy assessments increasingly emphasize geothermal energy as a vital baseload asset with growing strategic importance in future low-carbon energy systems (Anatolitis et al., 2024).

The East African Rift System (EARS) is one of the world's most extensive continental rifts, stretching for over 4000 kilometers from southern Mozambique through Tanzania, Kenya and Ethiopia to join the Red Sea and Gulf of Aden rifts at the Afar triple junction. Rift development is associated with crustal extension, normal faulting, lithospheric thinning and spatially variable magmatism. The interaction between tectonic structures and magmatic activity has produced numerous volcanic centers, elevated heat flow and geothermal systems, particularly along the eastern branch of the rift system (Mibei, 2021; Chorowicz, 2005). The Kenya rift system is a crucial segment of the EARS; it functions as a tectonically divergent zone under tensile forces, creating numerous surface and buried structural faults (Omollo et al., 2022; Omenda, 2010). According to Biggs et al. (2016, 2009), recent data such as the high rate of seismicity, evidence of high surface heat flow, recent volcanism, and more recent inflation incidents at some of the volcanoes, show that the Kenya rift is still active. The focus of this study is the Korosi field, a prominent geothermal system situated within the northern sector of the Kenya rift shown in **Figure 1**.

Korosi is a trachyte-basalt volcanic complex situated north of Lake Baringo. It is positioned within the inner trough of the rift, characterized by Quaternary volcanism at its center and bounded by thick sedimentation to the east and west (Dunkley et al., 1993). The geothermal surface manifestations at Korosi include fumaroles, hot and thermally altered grounds, and high-temperature water boreholes. These features are predominantly aligned along north to north-northeast trending faults, highlighting the structural control on fluid flow within the system (Ochieng et al., 2012). This study was therefore undertaken to investigate the subsurface structure to delineate the reservoir, heat source, and the specific geological structures such as these faults that govern the hydrothermal system.

Geophysical exploration of the geothermal system is generally carried out to image the subsurface structure of the reservoir and its major aim is to determine the depth and dimensions of the reservoir as well as to identify the location of the heat source (van Leeuwen, 2016). Munoz (2014) identifies subsurface electrical conductivity as a vital parameter for characterizing geothermal settings. These systems consist of intricate fault and fracture networks saturated with saline fluids, which function as conductive electrolytes within the host rock.

Subsurface environments characterized by elevated temperatures, high salinity, and interconnected fluid networks typically manifest as pronounced high conductivity anomalies (Kana et al., 2015). These low-resistivity signatures are often indicative of hydrothermal reservoirs or, at greater depths, the presence of partial melts and high-temperature magmatic bodies. The resultant low-resistivity anomalies have been the primary target for the geophysical exploration of geothermal resources (Simpson & Bahr, 2005).

The Magnetotelluric method is a passive electrical method for geophysical exploration that uses temporal fluctuations of the Earth's electromagnetic field to remotely sense the electrical properties of the subsurface (Chave & Jones, 2012). Due to its superior depth of investigation and sensitivity to conductivity gradients, MT has become the primary tool for delineating geothermal targets and identifying the transition between conductive alteration zones and resistive host rocks.

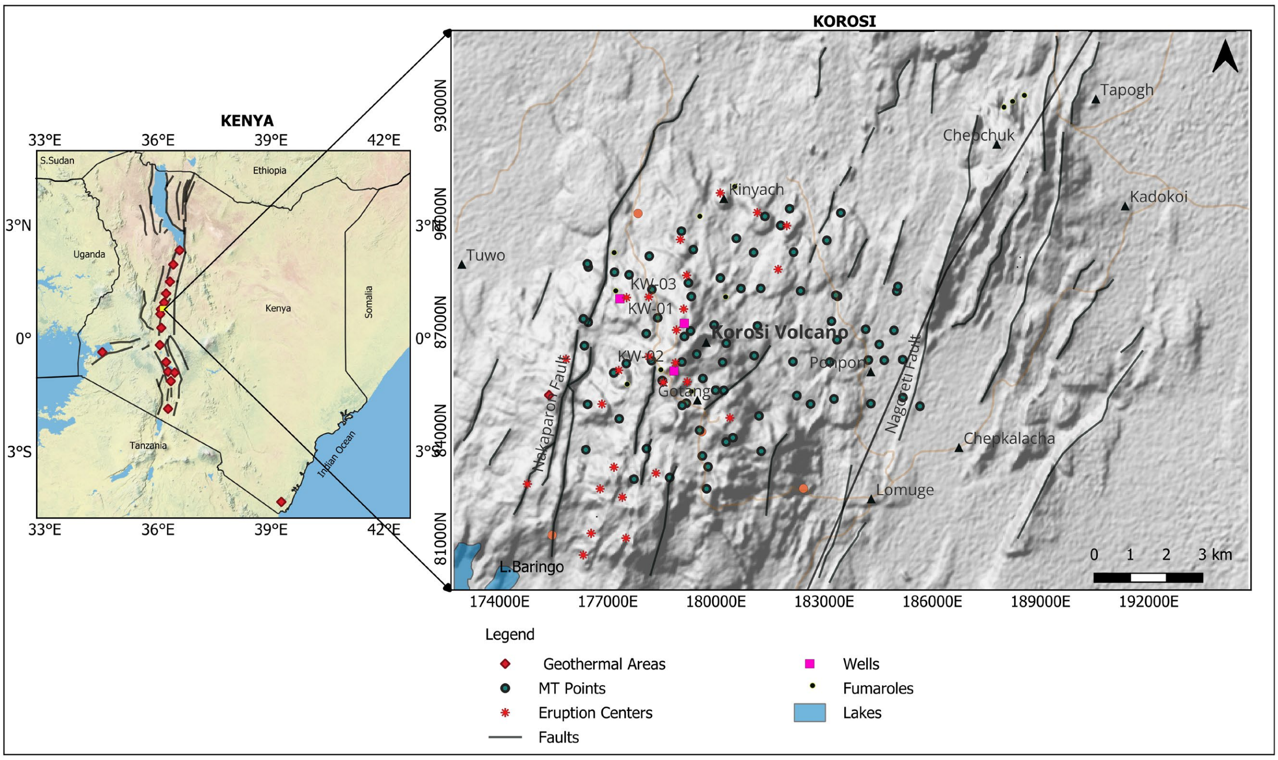

Figure 1. Map of Korosi geothermal prospect, Baringo, Kenya.

2. Geology

Korosi is a multi-vent complex built mainly of trachyte lavas that form a low shield, with minor amounts of basalt, mugearite and pyroclastic deposits as in Figure 2.

The oldest exposed rocks of the volcanic complex are pumiceous air-fall deposits that cover a large area to the west and south-west of Korosi, on the flat ground around Loruk and extending northwards to the plain of Korkore. The Lower trachytes are exposed in a peripheral apron around the outer flanks of Korosi and rest upon pumiceous deposits on the south-west. A major episode of fissuring and faulting accompanied and controlled the eruption of basalts and mugearites. These rocks occur in three main areas: a large part of the southern and south-western flanks extending into Lake Baringo, the peripheral northern flanks and the low ground between Korosi and Paka, and a minor occurrence on the western side of the summit area near Lemu (Dunkley et al., 1993).

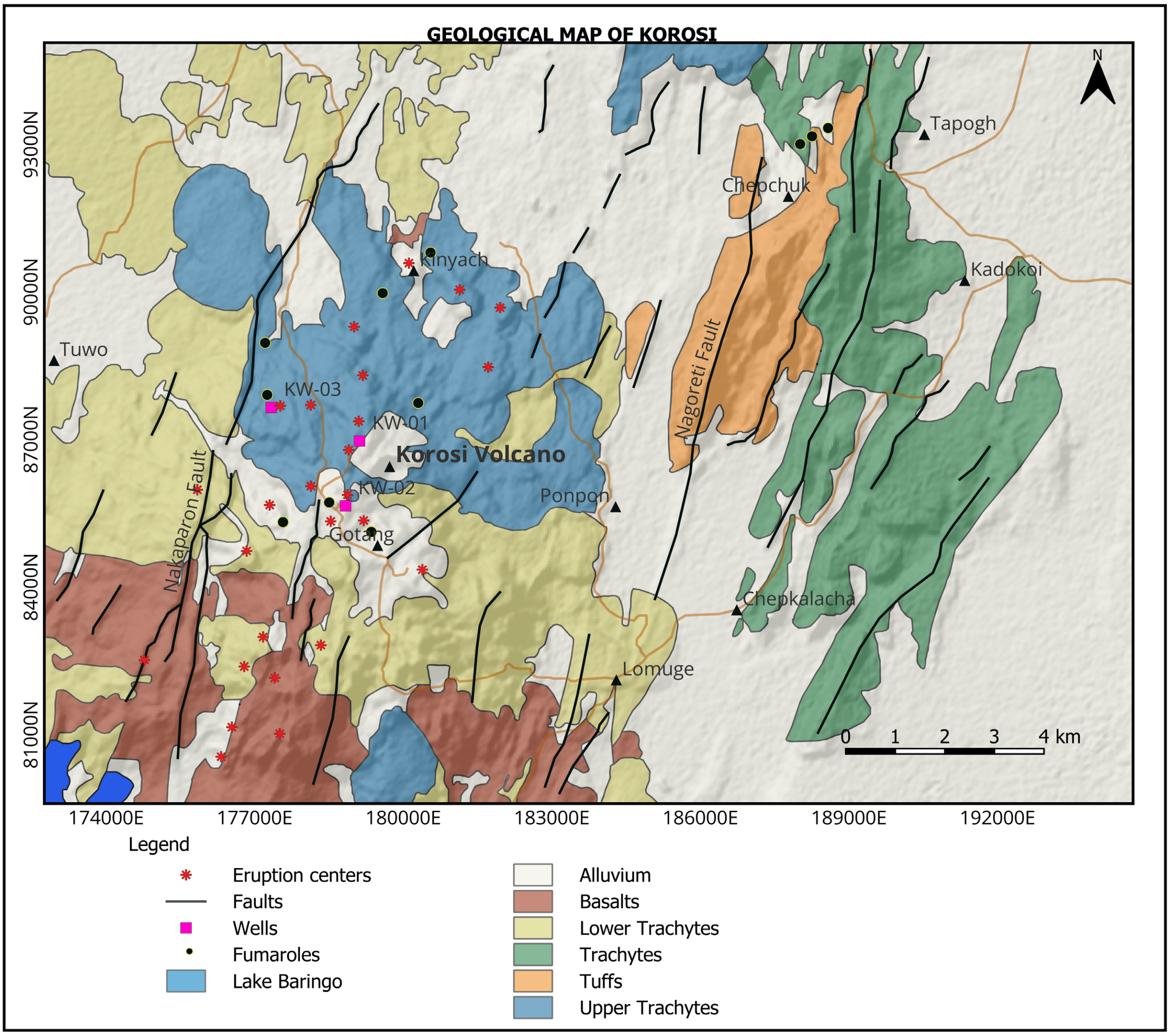

Figure 2. Geological map of Korosi geothermal prospect.

Upper trachytes cover large part of northern flanks, overlying lower trachytes, basalts and mugearites and are generally less faulted. Extrusive domes occur on the periphery of the northern flanks, with lavas extruded from breaches and also on the upper flanks, such as on the north-west side of the summit area. Small parasitic domes occur on the surfaces of several Upper Trachyte flows, including a northeast trending line a short distance northeast of Getang crater and a parallel line to the northwest. These are oriented parallel to the main faults, suggesting control by underlying fractures. The youngest activity is represented by very young, unvegetated basalts in the Adomeyon area (Dunkley et al., 1993).

Structural deformation within the Korosi volcanic complex is generally characterized by faults with relatively minor displacement. However, several major fault systems located to the eastern and western margins of the complex define a broad graben structure that hosts the volcanic edifice. Satellite imagery clearly reveals numerous faults and fissures surrounding the Korosi volcanic complex. The orientation trend is strongly pronounced in a north-northeast to south-southwest direction with the major bounding faults being Nakaporon to the west and Nagoreti to the east (Njue, 2014).

The Nakaporon fault zone represents the most significant area of surface geothermal activity at Korosi. The fault zone is strongly associated with the Nakaporon fault system and is marked by a prominent escarpment and hanging-wall structures developed at the intersections of north-northeast and east-trending faults. Geothermal manifestations are concentrated within trachytic rocks in the southern sector and basaltic lavas and mafic intrusions in the northern sector. Surface expressions include widespread steaming ground, fumaroles, and steam seepages, many of which are relatively large and vigorous. Hydrothermal alteration is extensive and includes red argillic zones, carbonate veining, and silicification (Dunkley et al., 1993). Sinter is found at the locations of former hot springs, indicative of a higher local water table in the recent past.

3. Methodology

3.1. Magnetotelluric Method

The magnetotelluric method is a passive electrical method for geophysical exploration that uses temporal fluctuations of the Earth's electromagnetic (EM) field to remotely sense the electrical properties of the subsurface (Chave & Jones, 2012). Two electric field components (E_x , E_y) and three magnetic field components (H_x, H_y, H_z) are measured at each MT station. The frequency-dependent impedance tensor (*Z*), which is the ratio of orthogonal electric and magnetic components measured at the Earth's surface, can be used to determine the electrical properties of the subsurface as a function of depth (Cagniard, 1953):

$$\begin{bmatrix} E_x \\ E_y \end{bmatrix} = \begin{bmatrix} Z_{xx} & Z_{xy} \\ Z_{yx} & Z_{yy} \end{bmatrix} \begin{bmatrix} H_x \\ H_y \end{bmatrix} \tag{1}$$

where Z_{xx}, Z_{xy}, Z_{yx} and Z_{yy} are elements of the impedance tensor Z and are also complex magnitudes.

The complex impedance tensor with real and imaginary parts in the frequency domain can be expressed in terms of the apparent resistivity and phase:

$$\rho_{aij} = \frac{1}{\mu\omega}\left|Z_{ij}(\omega)\right|^2 \tag{2}$$

where the subscripts i and j are indexes for the rows and columns of the impedance tensor. The apparent resistivity represents the average resistivity of the subsurface at a particular frequency. The phase in degrees describes the phase difference between the electric and magnetic field giving additional information on resistivity structure (Simpson & Bahr, 2005):

$$\Phi_{ij} = \arctan\left(\frac{\mathrm{Im}\left(Z_{ij}(\omega)\right)}{\mathrm{Re}\left(Z_{ij}(\omega)\right)}\right) \tag{3}$$

3.2. MT Data Acquisition and Processing

The MT data used in this study were acquired by a team from Geothermal Development Company (GDC) between 2011 and 2022. A total of 81 MT sounding datasets, shown as green dots in **Figure 3** were used for this study. The stations were selected to provide coverage across the western, central and eastern parts of the Korosi geothermal field, while accounting for terrain accessibility and avoiding sources of cultural and electromagnetic noise. The nearest neighbor station spacing ranged from approximately 0.06 to 1.26 km, with denser coverage in the central part of the field and comparatively wider spacing towards the margins where access was more limited. This distribution provided sufficient spatial coverage for evaluating lateral resistivity variations across the principal parts of the geothermal field.

Data were acquired using Phoenix MTU-5A 24-bit data logger, non-polarizing porous pot electrodes and three induction coils. At each sounding station, five channels of data were recorded simultaneously: two orthogonal horizontal electric field components (E_x, E_y) and three magnetic field components (H_x, H_y, H_z). The electric field was measured using two 60 meter electrodes configured in a cross layout, oriented to magnetic north-south and east-west, with non-polarizing electrodes buried in shallow pits to ensure stable electrical contact with the subsurface. The magnetic field component was measured using three induction coils; the horizontal coils (H_x, H_y) were aligned with the electrodes, while the vertical coil (H_z) was vertically buried in the ground. At each station, data were recorded for approximately 18 hours to provide sufficient time for resolving long period MT responses and to include nighttime intervals, when cultural electromagnetic noise is generally reduced and natural field signal quality may improve.

The raw time-series data were subsequently processed using the SSMT2000 software manufactured by Phoenix Geophysics, which utilizes robust Fourier transformation techniques to convert time-domain signals into the frequency domain, ultimately yielding apparent resistivity and impedance phase curves. Following robust processing in SSMT2000, the MT plot files were imported into Phoenix MT Editor for quality control. Apparent resistivity and phase curves were examined together with the individual cross-powers that are used to calculate each point on the curves. Automatic editing was initially applied and subsequently refined through manual inspection. Cross-powers affected by excessive scatter, poor coherence, cultural interference or inconsistent behavior were excluded, while reliable estimates were retained or restored. The edited responses were exported in Electronic Data Interchange (EDI) format for dimensionality analysis and three dimensional inversion. No complete station or continuous frequency band was rejected, only individual unreliable cross-powers or frequency estimates were excluded and all 81 stations were retained for dimensionality analysis and three-dimensional inversion. The final inversion dataset contained 80 frequencies covering 0.001 - 320 Hz.

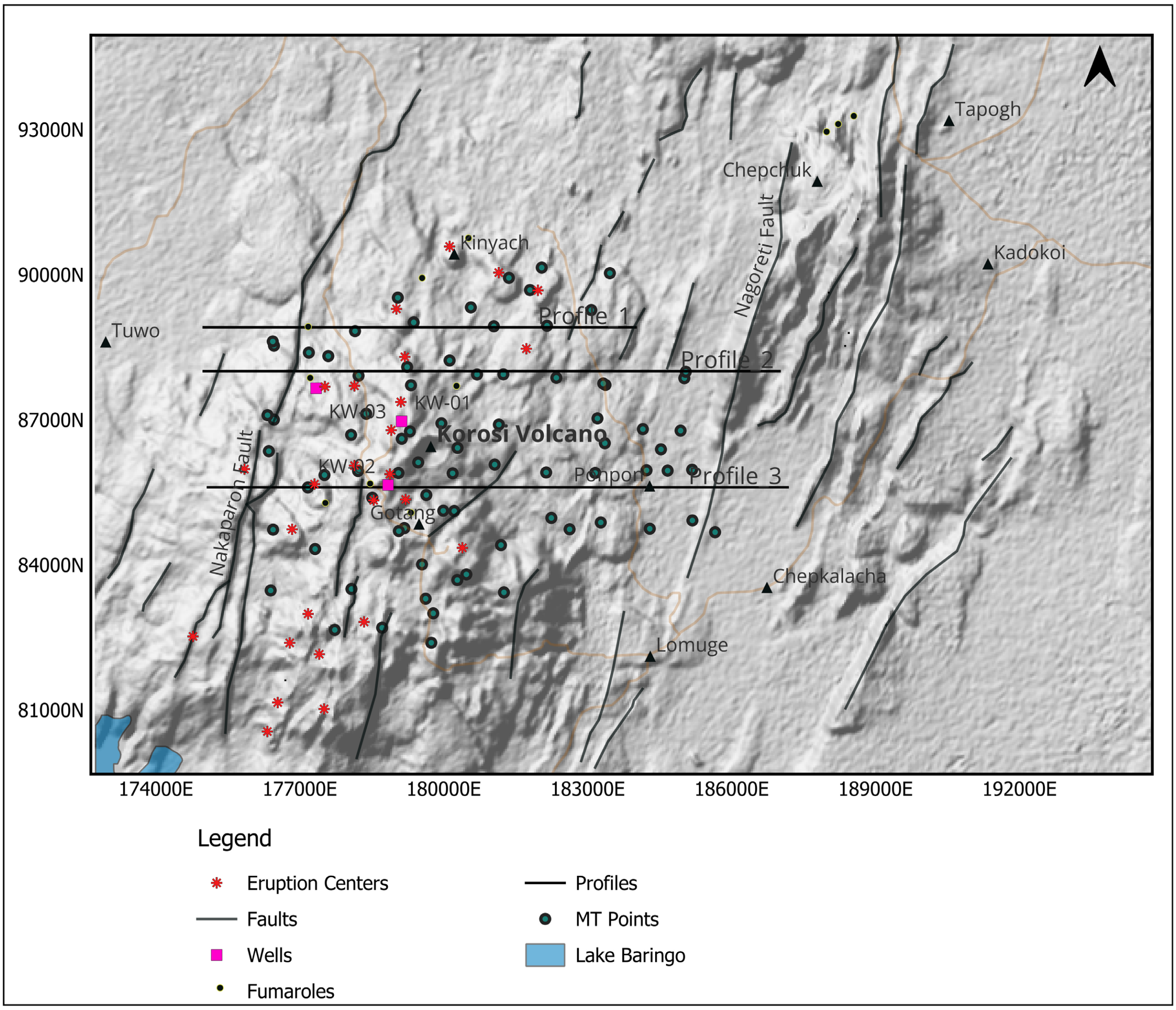

Figure 3. Profiles overlain of the Korosi geothermal field with the location of MT data stations on DEM map. The profile lines used to extract vertical sections from the three dimensional resistivity model are also shown.

Although the measurements were collected during several survey campaigns between 2011 and 2022, the datasets were prepared using a common coordinate convention and were converted to a consistent impedance format before inversion. Electrode and magnetic coil orientations, impedance signs, frequency sampling and units were checked during compilation. Instrument calibration information contained in the original datasets was retained during processing. This enabled the different survey campaigns to be incorporated into one internally consistent dataset.

3.3. Dimensionality Analysis of MT Data

Prior to MT modelling, dimensionality analysis was performed to evaluate whether the computed impedance tensors, apparent resistivities and phases from observed data at selected frequencies reflect one dimensional (1D), two dimensional (2D) or three dimensional (3D) geoelectrical structures.

It also enables the identification and quantitative assessment of galvanic and inductive distortions (Groom & Bailey 1991; McNeice & Jones, 2001) and allows the recovery of subsurface strike directions (Martí et al., 2010). This step is essential for selecting the most representative modelling approach for a given MT dataset. In this study, we applied the phase tensor technique (Caldwell et al., 2004; Booker, 2014) to determine if the local geo-electric environment is best characterized by a 1D, 2D, or 3D resistivity model.

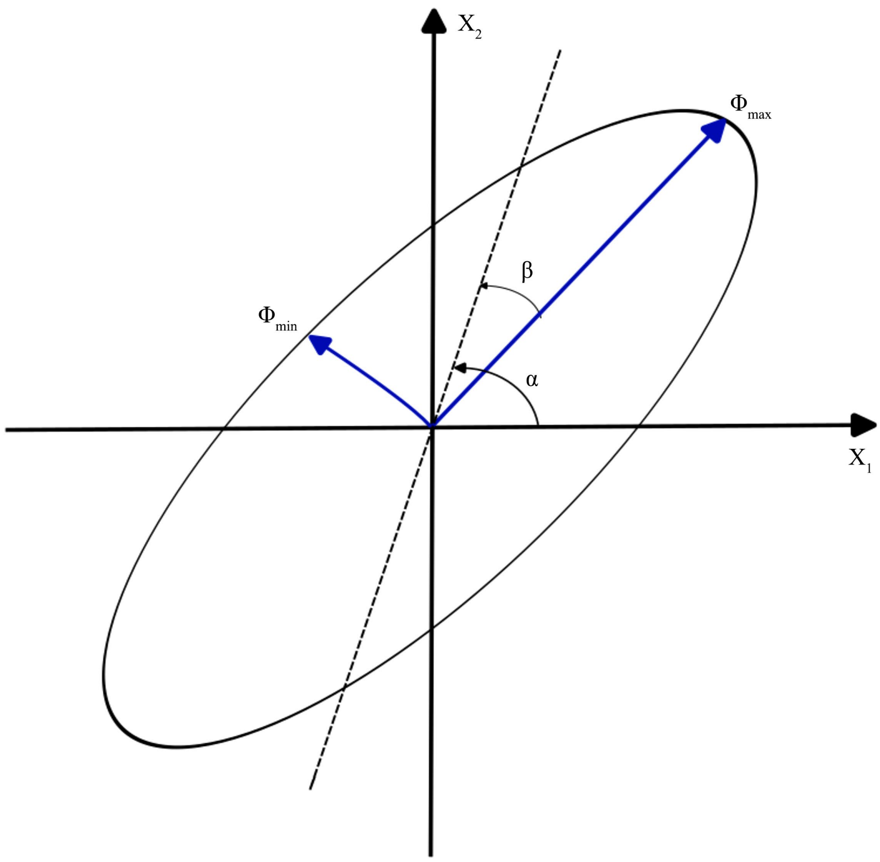

Figure 4. The phase tensor plotted graphically as an ellipse. The major and minor axes of the ellipse depict the principal axes and values of the tensor with the orientation of the major axis specified by the angle α-β.

As an essential tool for assessing subsurface geoelectric dimensionality, the phase tensor enables the visualization of lateral changes in the regional conductivity structure at different depths via frequency-dependent ellipse maps and remaining entirely unaffected by galvanic distortion caused by small-scale, unresolvable surface structures (Bibby et al., 2005; Booker, 2014; Caldwell et al., 2004).

Mathematically defined as the product of the inverse real and the imaginary matrix of the impedance tensor, the phase tensor captures the regional-scale inductive response without requiring prior assumptions about the nature of the subsurface conductivity distribution. It is applicable where both the heterogeneity and the regional conductivity structures are 3D.

Graphically, the tensor is represented as an ellipse characterized by its maximum ($\Phi_{\max}$) and minimum ($\Phi_{\min}$) axes representing the principal axes of the tensor as shown in **Figure 4**. The third coordinate invariant, the skew angle (β), quantifies the degree of asymmetry in the phase tensor and it is the primary indicator used to distinguish between 2D and 3D subsurface structures (Caldwell et al., 2004). If the skew angle is small (<3˚) and has low ellipticity (circular) this indicates 1D or 2D geoelectric structures whereas large skew angles indicate the presence of a 3D regional structure.

3.4. 3-D MT Data Inversion

The objective of a 3D MT inversion is to produce a 3D resistivity model consistent with MT data that require it (Maithya & Fujimitsu, 2019). The 3D MT data inversion was carried out using the 3D ModEM code (Egbert & Kelbert, 2012; Kelbert et al., 2014; Meqbel, 2009). The use of 3D inversion is particularly important in structurally complex geothermal systems, where 1D and 2D assumptions may oversimplify resistivity boundaries and reservoir geometry (Spichak & Manzella, 2009; Omollo et al., 2022).

ModEM code for 3D inversion is based on the minimization of the problem of penalty function effect by the parallelized nonlinear conjugate gradient represented by Equation (4).

$$U(m,d)=\left(d-F(m)\right)^{\mathrm{T}} C_d^{-1}\left(d-F(m)\right)+\lambda\left(m-m_0\right)^{\mathrm{T}} C_m^{-1}\left(m-m_0\right) \qquad (4)$$

The first term in Equation (4) represents the data misfit between the measured (d) and model response $F(m)$. m and m_0 are the initial and estimated model, respectively. C_d and C_m are the data and model covariances whereas λ is a trade-off parameter between data misfit and model structure. The initial model, m_0 is updated iteratively by line search strategy and the 3D forward scheme is based on finite differences, and the inverse scheme exploits the nonlinear conjugate gradient method.

A total of 81 MT data soundings were used for 3D inversion and a starting model of 50 Ωm half-space was applied for the inversion. In the vertical z direction, 48 layers were used with the first layer thickness of 10 m subjected to an increasing factor of 1.1. The x direction was padded with four cells with an increasing factor of 1.1. The y direction was also padded with five cells with an increasing factor of 1.1. The resultant model was 9.6 km in depth with 68 × 85 × 48 cells in x, y and z direction. The 3D inversion process used all four components of the impedance tensor data with error floors of 5% of $\sqrt{\left(\left|Z_{xy} \times Z_{yx}\right|\right)}$ for all components for all sites. The inversion reduced the normalized root-mean square (RMS) misfit from 21.4 to 4.07 after 34 iterations.

Surface topography was not explicitly incorporated into the inversion mesh and the model therefore employed a flat surface approximation. Lake Baringo was also not represented as a separate conductive water body or included explicitly in the model boundary conditions. Consequently, shallow resistivity variations near areas of pronounced relief and towards the Lake Baringo margin may partly reflect simplifications associated with the model geometry. Interpretation in these areas was therefore undertaken cautiously, with greater emphasis placed on laterally persistent and deeper resistivity structures.

4. Results and Discussion

4.1. Phase Tensor Maps

The overall complexity of the subsurface structure beneath Korosi geothermal area was evaluated using MT phase tensor at different periods shown in **Figures 5-7** in which the phase tensor ellipses are colored by their skew angles. These specific period intervals were targeted to optimize resolution across the reservoir zone, as they successfully capture the transition into more pronounced 3D geoelectric behavior. The dimensionality of the subsurface structures can be inferred from the shapes of the phase tensor and skew angle. **Figure 5** shows ellipses at short periods (0.1 s) and a significant amount of the ellipses in the survey area are quite generally circular, yellow in color and show relatively small skew angles ($-3^\circ < \beta > 3^\circ$) exhibiting a 1D characteristic, whereas some few stations indicate 2D (elliptical with $\beta < 3^\circ$) implying structures at shallow depths mostly have 1D and 2D characteristics.

The phase tensor analysis at period 1 second in **Figure 6**, shows that most of the stations exhibit a more complex aspect that points to 3D effect characterized by a high skew angle (elliptical with $\beta > 3^\circ$) whereas some few stations indicate 2D (elliptical with $\beta < 3^\circ$) dimensionality. For longer periods in **Figure 7**, clear characteristics of the 3D structure are shown (elliptical with $\beta > 3^\circ$). Generally, the phase tensor analysis shows a complex scenario in which 1D and 2D dimensionality effects are prominent at shallow depth whereas 3D characteristics are detected at deeper levels.

At different depths, the directions of the observed induction arrows, in Parkinson convention (Parkinson, 1959), are heterogeneous, implying complexity in the distribution of the conductive structures. The phase tensor results clearly show that the subsurface is complex electrically and therefore 3D data inversion is needed.

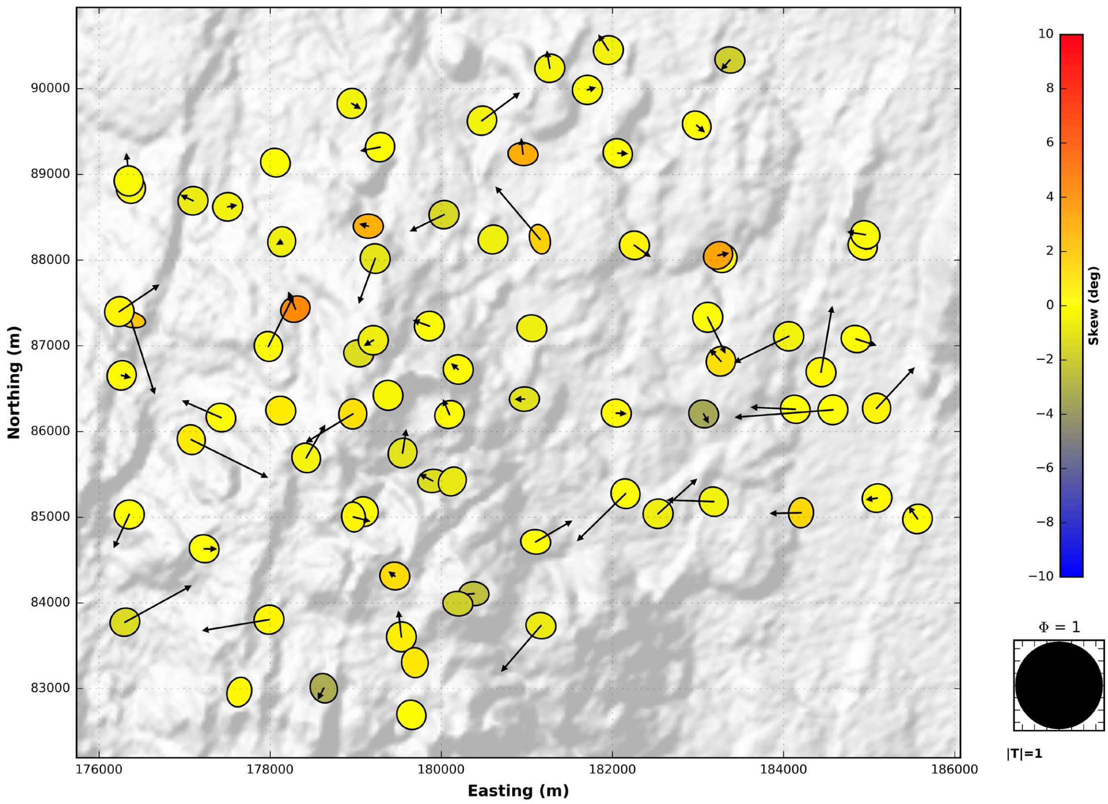

Figure 5. Phase tensor ellipses in the Parkinson convention for a period of 0.1 seconds.

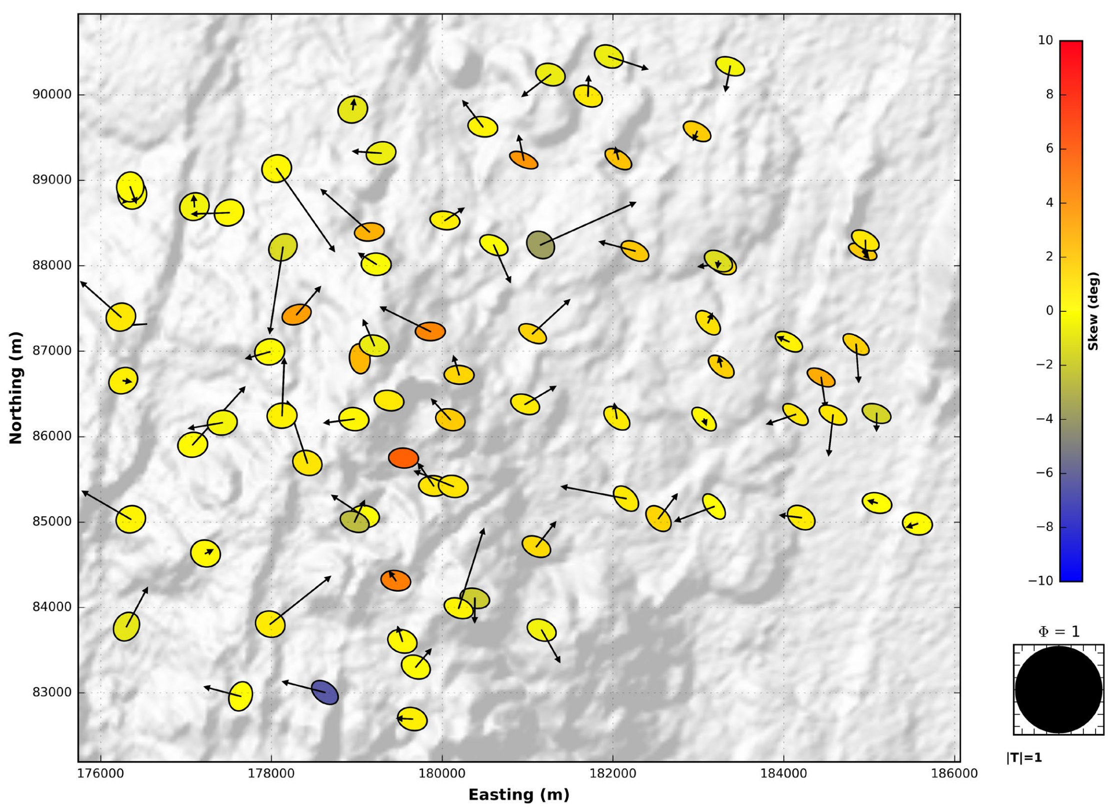

Figure 6. Phase tensor in the Parkinson convention for a period of 1 second.

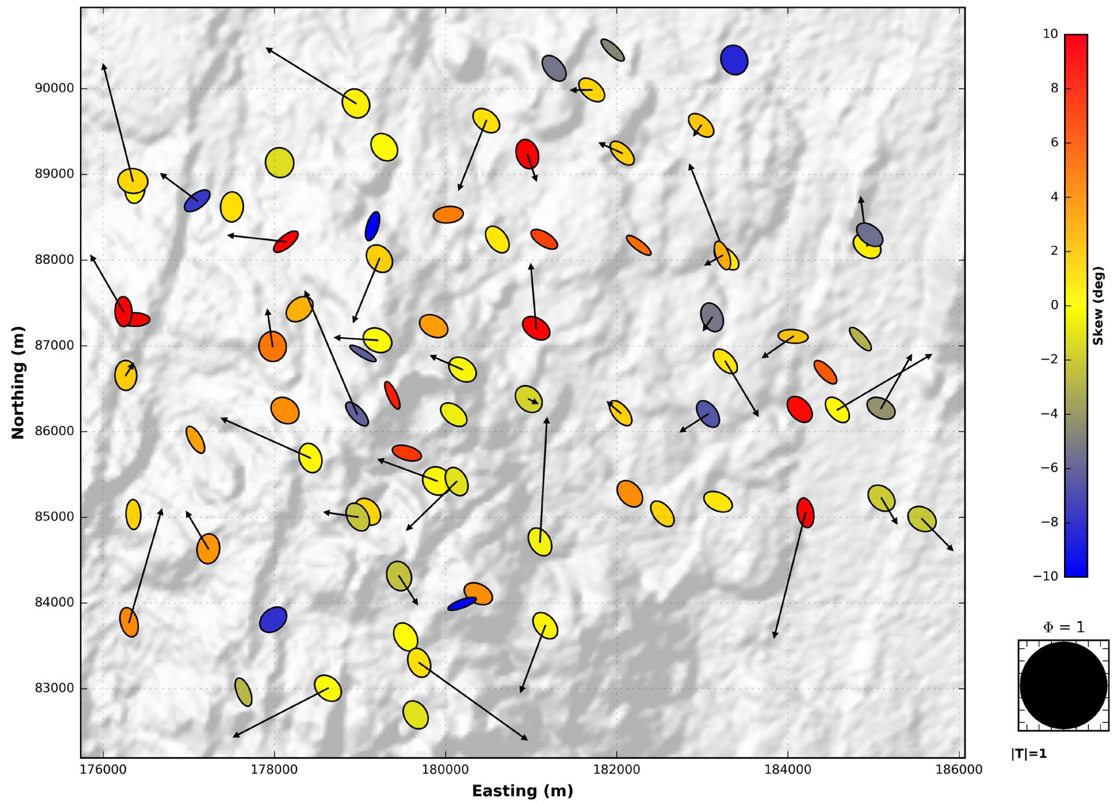

Figure 7. Phase tensor ellipses in the Parkinson convention for a period of 10 seconds.

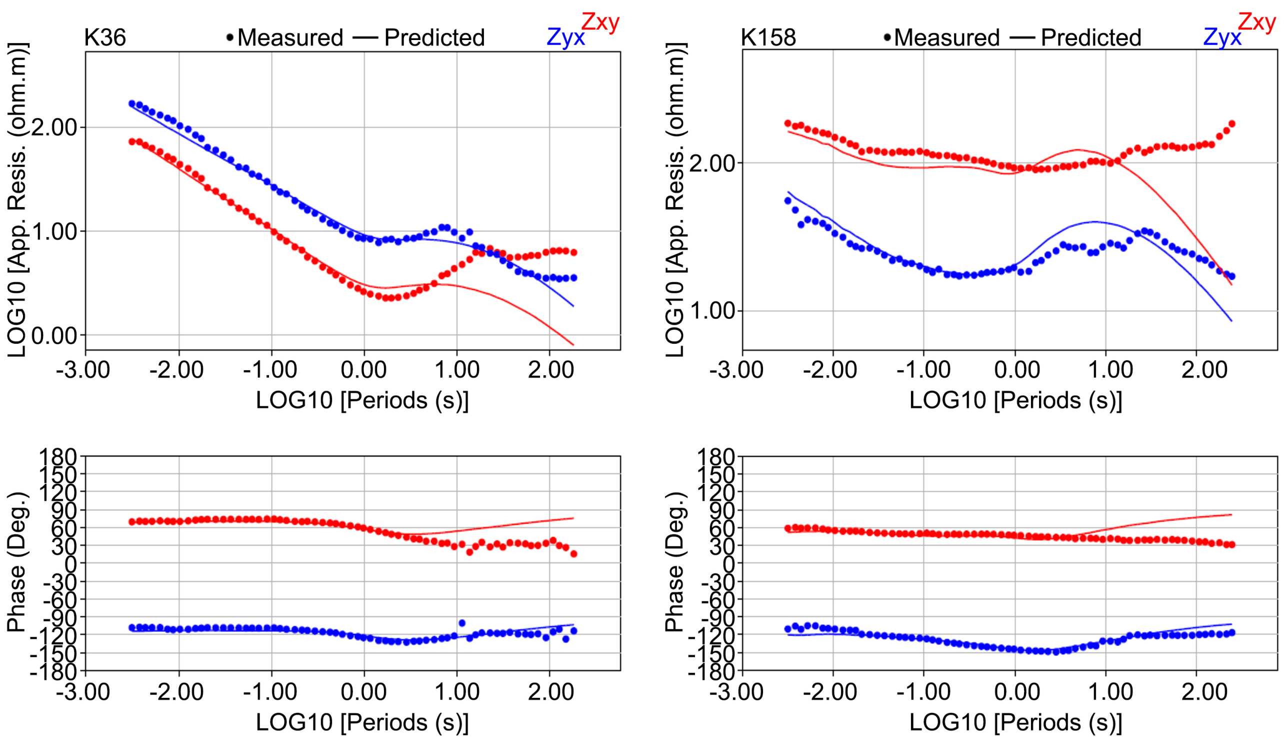

Figure 8. Comparison of measured and predicted MT responses at stations K36 and K158. Dots represent measured data and continuous lines represent responses predicted from the final ModEM model. The upper panels show apparent resistivity and the lower panels show impedance phase.

4.2. Data Misfit (Observed vs Calculated)

The quality of the final inversion was assessed by comparing the measured impedance responses with the responses predicted by the recovered three dimensional resistivity model. Figure 8 presents representative apparent resistivity and phase fits for stations K36 and K158. The predicted responses reproduce the principal trends in the measured apparent resistivity and phase, particularly at short and intermediate periods. Some discrepancies occur at longer periods and vary among stations and impedance components, indicating reduced model fit for parts of the deeper response. Overall, the comparison demonstrates that the final 3D model captures the main resistivity structure of the Korosi geothermal field.

4.3. 3-D Inversion Results

Three west-east resistivity cross-sections extracted from the final 3D inversion model are presented in Figures 9-11. Slices are shown to a maximum depth of 5 kilometers, since there are no significant structures towards greater depths and they image the resistivity distribution beneath the Korosi geothermal field. Although each profile exhibits local variations in geometry, all three display a similar resistivity architecture consisting of a shallow resistive layer, an extensive conductive zone and a deeper resistive body. Conductive (C) and resistive (R) anomalies are labelled independently in each profile for ease of description.

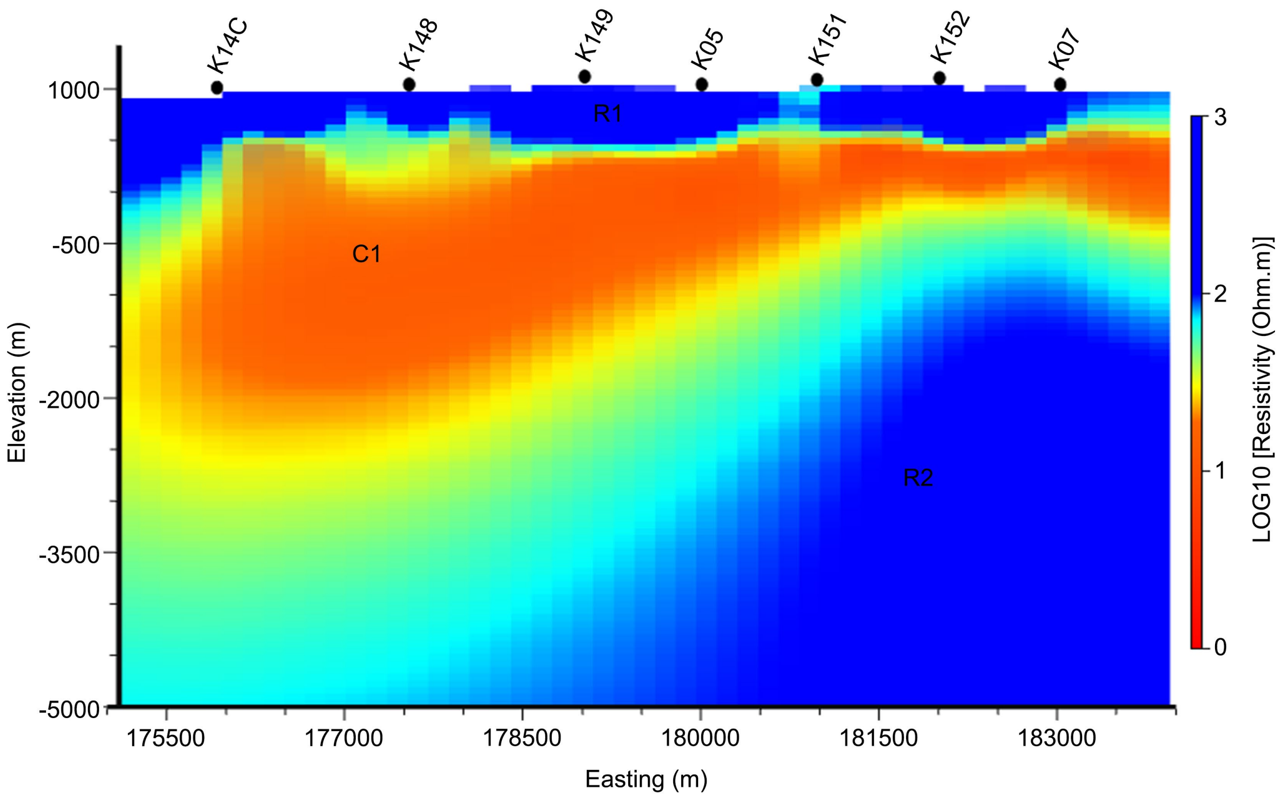

Figure 9. 3D resistivity model through Profile 1.

Profile 1 crosses the northern part of the study area as shown in Figure 9. A thin resistive uppermost layer (R1) occupies the near-surface throughout the profile with resistivity values generally exceeding 100 Ωm. The uppermost layer is underlain by a broad conductive anomaly (C1) with resistivity values below approximately 10 Ωm occupying the entire length of the profile. The conductor reaches its greatest thickness beneath the western part of the section, extending to approximately 2200 m below sea level (b.s.l) before gradually thinning eastward. Underlying C1 is a large resistive body (R2) with resistivity values exceeding 100 Ωm. The resistive body deepens toward the western part of the profile but rises progressively toward the east, where its upper boundary becomes significantly shallower beneath the eastern side of the profile.

Figure 10 shows Profile 2 and it comprises a thin near-surface resistive layer (R3), two conductive anomalies (C2 and C3) and a deep resistive body (R4). Conductor C2 occupies the western portion of the profile and extends from the near surface to approximately 2,300 m b.s.l. A second conductor (C3) occurs beneath the eastern part of the profile and is separated from C2 by a zone of relatively higher resistivity. The deep resistive body R4 underlies both conductive anomalies and occupies most of the lower half of the profile. The upper surface of R4 rises gradually toward the eastern part of the section.

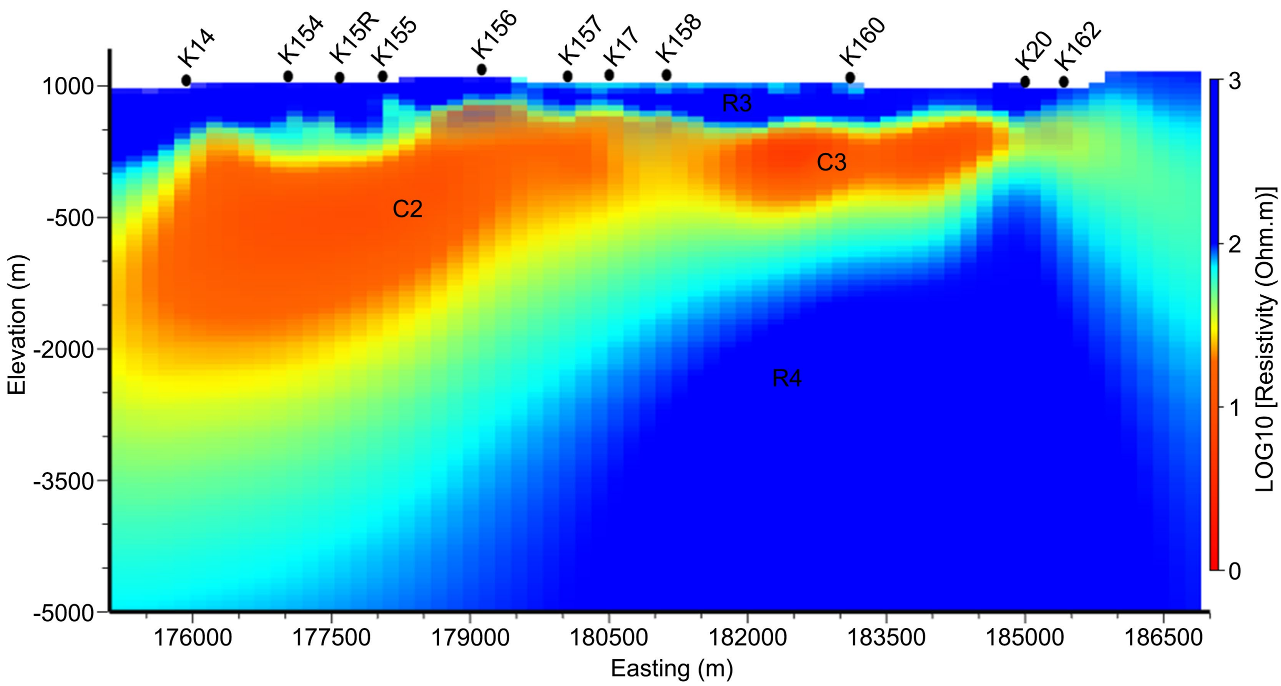

Figure 10. 3D resistivity model along Profile 2.

Profile 3, the southernmost profile, is presented in Figure 11. A thin, laterally continuous high-resistivity layer (R5) occurs near the surface throughout the profile, with resistivity values generally exceeding 100 Ωm. A conductor (C4) with resistivity values generally below 10 Ωm extends from near the surface to approximately 1800 m b.s.l. Exploration well KW-02 is situated close to the eastern boundary of conductive anomaly C4. Conductive anomaly C5 occurs in the eastern part of the profile where it extends from near the surface to depths of approximately 1800 m b.s.l. C5 is separated from the western conductor (C4) by a resistive zone occupying the central part of the profile. The lower part of the profile is dominated by a large high-resistivity body (R6) occupying depths from approximately 1800 m b.s.l.

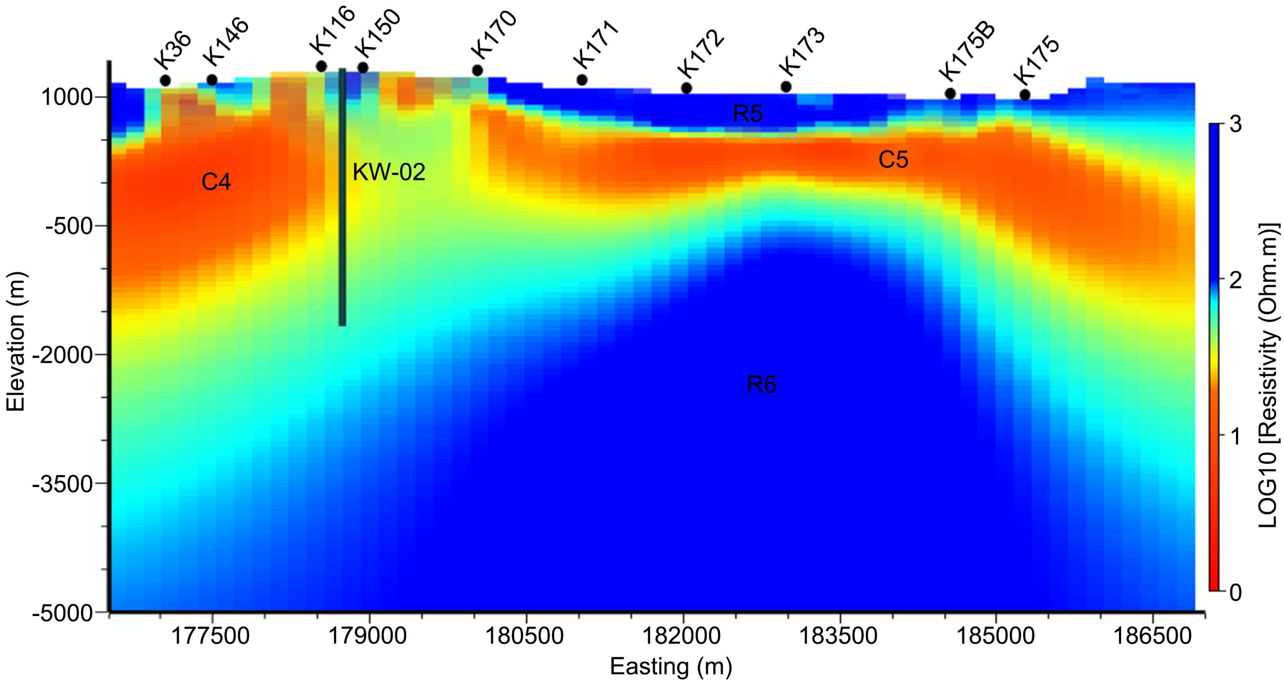

Figure 11. 3D resistivity model along Profile 3 cutting through Korosi well KW-02.

4.4. Discussion

The 3D MT inversion model of the Korosi geothermal field images a broadly consistent three layer resistivity structure across the three west-east profiles. This consists of a thin, near-surface high resistivity layer (>100 Ωm), a laterally extensive conductive zone with resistivity values generally below 10 Ωm, and a deeper resistive body with resistivity values commonly exceeding 100 Ωm. Similar resistivity patterns are widely reported in volcanic hosted geothermal systems, where a conductive clay cap overlies a more resistive deeper zone (Maithya & Fujimitsu, 2019; Lichoro et al., 2019, 2017; Ussher et al., 2000).

The thin, laterally continuous near surface resistive layer imaged at the top of all three profiles is interpreted as relatively unaltered, dry or weakly altered volcanic rocks above the main hydrothermal alteration zone. At Korosi, this layer is likely associated with recent, well drained tuffs and lava units that form part of the volcanic edifice. Its high resistivity is consistent with limited clay alteration and reduced pore fluid connectivity in the shallow subsurface (Dunkley et al., 1993; Lichoro et al., 2017).

The conductive bodies C1 - C5, with resistivity values generally below 10 Ωm, are interpreted as components of the hydrothermal clay cap. This low resistivity zone is most likely produced by smectite- and zeolite-rich alteration of tuffs and other permeable volcanic units. Such alteration is common in the lower temperature parts of volcanic geothermal systems, where smectite and mixed-layer clays strongly reduce bulk resistivity. With increasing temperature and depth, smectite-rich assemblages are commonly replaced by more resistive illite, chlorite and locally epidote-bearing alteration minerals, producing a transition from the conductive clay cap into a more resistive deeper zone (Savitri et al., 2022; Revil & Gresse, 2021; Fulignati, 2020).

The western conductors C1, C2 and C4 form the most laterally persistent conductive feature in the model, suggesting that the clay alteration zone is continuous along the western part of the field. Their repeated occurrence across the three profiles indicates that this conductive zone is unlikely to be an isolated anomaly, but rather a coherent hydrothermal alteration feature. Where eastern conductors are imaged, particularly C3 on Profile 2 and C5 on Profile 3, they are separated from the western conductive zone by a relatively resistive central block. This geometry suggests lateral compartmentalization of the alteration system, possibly controlled by structural or lithological variations. However, the presence of separate conductive zones should not be interpreted directly as evidence for separate reservoirs without supporting temperature, permeability and geochemical data.

A relatively resistive zone is imaged beneath the conductive clay cap in all three MT profiles. The deeper resistive bodies R2, R4 and R6 therefore represent key features of the inversion model, although their geological meaning remains non-unique. In volcanic geothermal systems, the transition from a conductive clay cap to a deeper resistive zone is commonly associated with increasing temperature and the replacement of smectite-rich alteration by illite, chlorite and locally epidote-bearing assemblages. Such a transition may indicate reservoir level conditions. However, high resistivity at depth does not necessarily confirm the presence of a productive geothermal reservoir, because similar resistive signatures may also result from dense intrusive rocks, low-porosity lava units, relict alteration zones or basement lithologies (Cumming & Mackie, 2010; Lichoro et al., 2019).

The KW-02 well provides an important qualitative constraint on the Profile 3. Its position near the eastern margin of conductor C4, close to the central resistive block between C4 and C5, allows comparison between the MT model and available drilling observations. Although the well indicates the presence of permeable zones, the available temperature information does not confirm high-temperature reservoir conditions at the drilled location. Therefore, the C4 resistive transition should be interpreted as a permeable but not necessarily high temperature zone, at least where it is intersected by KW-02.

5. Conclusion

The 3D MT inversion results reveal a consistent resistivity structure beneath the

Korosi geothermal field, comprising a shallow resistive layer, an extensive conductive clay cap zone and deeper resistive bodies. The conductive anomalies C1 - C5 are interpreted as hydrothermal clay alteration zones, most likely associated with smectite- and zeolite-rich alteration of permeable volcanic units. Their distribution suggests that hydrothermal alteration is laterally variable and may be influenced by structural or lithological controls.

The deeper resistive bodies R2, R4 and R6 represent important components of the subsurface resistivity structure and may mark the transition into higher-temperature alteration assemblages dominated by illite, chlorite and locally epidote. However, these resistive zones are not uniquely diagnostic of productive geothermal reservoirs, since similar resistivity responses may also be produced by dense intrusive rocks, low-porosity lava units, relict alteration or basement lithologies. The qualitative constraint from KW-02 further indicates that permeability may occur along the C4 resistive body transition, but high temperature reservoir conditions are not confirmed at the drilled location.

The interpretation presented here therefore emphasizes broad and spatially continuous structures supported by several neighboring stations, particularly the extensive conductive alteration zones and the upper boundaries of the deeper resistive bodies. Future inversion should incorporate surface topography and the conductive effect of Lake Baringo to assess the robustness of shallow features near the survey margins.

Overall, the MT results support the presence of a well-developed hydrothermal alteration system at Korosi, with the most prospective zones likely occurring where deeper resistive bodies coincide with major structures, sustained permeability and independent evidence for elevated temperatures. Future exploration should therefore integrate the MT model with structural mapping, geochemistry, seismicity and additional well data to better distinguish productive reservoir zones from non-reservoir resistive bodies.

Acknowledgements

Special thanks to the Geothermal Development Company (GDC), Kenya, for data support. We acknowledge the support from the Department of Physics at the Jomo Kenyatta University of Agriculture and Technology (JKUAT). We also thank Prof. Gary Egbert, Dr. Anna Kelbert and Dr. Naser Meqbel for the 3D ModEM inversion code. Additionally, we thank Dr. Naser Meqbel for the 3D Grid software used to create the model's input data.

Author Contributions

Claire Kimeli conducted data analysis, data interpretation, and prepared the original draft of the manuscript. Justus Maithya participated in data analysis, interpretation of the results, and manuscript review. Josphat Mulwa: Supervision, methodology review, data interpretation, and manuscript review. John Githiri: Supervision, methodology review, data interpretation, and manuscript review.

Conflicts of Interest

The authors declare no conflicts of interest regarding the publication of this paper.

References

Anatolitis, V., Bojek, P., Briens, F., Buisson, E., Criswell, T., Dallard, J., & Martinez, L. M. (2024). *The Future of Geothermal Energy*. International Energy Agency.

Bibby, H. M., Caldwell, T. G., & Brown, C. (2005). Determinable and Non-Determinable Parameters of Galvanic Distortion in Magnetotellurics. *Geophysical Journal International, 163,* 915-930. https://doi.org/10.1111/j.1365-246x.2005.02779.x

Biggs, J., Anthony, E. Y., & Ebinger, C. J. (2009). Multiple Inflation and Deflation Events at Kenyan Volcanoes, East African Rift. *Geology, 37,* 979-982. https://doi.org/10.1130/g30133a.1

Biggs, J., Robertson, E., & Cashman, K. (2016). The Lateral Extent of Volcanic Interactions during Unrest and Eruption. *Nature Geoscience, 9,* 308-311. https://doi.org/10.1038/ngeo2658

Booker, J. R. (2014). The Magnetotelluric Phase Tensor: A Critical Review. *Surveys in Geophysics, 35,* 7-40. https://doi.org/10.1007/s10712-013-9234-2

Cagniard, L. (1953). Basic Theory of the Magneto-Telluric Method of Geophysical Prospecting. *Geophysics, 18,* 605-635. https://doi.org/10.1190/1.1437915

Caldwell, T. G., Bibby, H. M., & Brown, C. (2004). The Magnetotelluric Phase Tensor. *Geophysical Journal International, 158,* 457-469. https://doi.org/10.1111/j.1365-246x.2004.02281.x

Chave, A., & Jones, A. (2012). *The Magnetotelluric Method: Theory and Practice*. Cambridge University Press.

Chorowicz, J. (2005). The East African Rift System. *Journal of African Earth Sciences, 43,* 379-410. https://doi.org/10.1016/j.jafrearsci.2005.07.019

Cumming, W., & Mackie, R. (2010). Resistivity Imaging of Geothermal Resources Using 1D, 2D and 3D MT Inversion and TDEM Static Shift Correction Illustrated by a Glass Mountain Case History. In *Proceedings World Geothermal Congress* (pp. 25-29). International Geothermal Association.

Dickson, M. H., & Fanelli, M. (2013). *Geothermal Energy: Utilization and Technology*. Routledge.

Dunkley, P. N., Smith, M., Allen, D. J., & Darling, W. G. (1993). *The Geothermal Activity and Geology of the Northern Sector of the Kenya Rift Valley*. British Geological Survey Research Report SC/93/1.

Egbert, G. D., & Kelbert, A. (2012). Computational Recipes for Electromagnetic Inverse Problems. *Geophysical Journal International, 189,* 251-267. https://doi.org/10.1111/j.1365-246x.2011.05347.x

Fulignati, P. (2020). Clay Minerals in Hydrothermal Systems. *Minerals, 10,* Article 919. https://doi.org/10.3390/min10100919

Groom, R. W., & Bailey, R. C. (1991). Analytic Investigations of the Effects of Near-Surface Three-Dimensional Galvanic Scatterers on MT Tensor Decompositions. *Geophysics, 56,* 496-518. https://doi.org/10.1190/1.1443066

Kana, J. D., Djongyang, N., Raïdandi, D., Nouck, P. N., & Dadjé, A. (2015). A Review of Geophysical Methods for Geothermal Exploration. *Renewable and Sustainable Energy Reviews, 44,* 87-95. https://doi.org/10.1016/j.rser.2014.12.026

Kelbert, A., Meqbel, N., Egbert, G. D., & Tandon, K. (2014). ModEM: A Modular System for Inversion of Electromagnetic Geophysical Data. *Computers & Geosciences, 66,* 40-53. https://doi.org/10.1016/j.cageo.2014.01.010

Lichoro, C. M., Árnason, K., & Cumming, W. (2017). Resistivity Imaging of Geothermal Resources in Northern Kenya Rift by Joint 1D Inversion of MT and TEM Data. *Geothermics, 68,* 20-32. https://doi.org/10.1016/j.geothermics.2017.02.006

Lichoro, C. M., Árnason, K., & Cumming, W. (2019). Joint Interpretation of Gravity and Resistivity Data from the Northern Kenya Volcanic Rift Zone: Structural and Geothermal Significance. *Geothermics, 77,* 139-150. https://doi.org/10.1016/j.geothermics.2018.09.006

Maithya, J., & Fujimitsu, Y. (2019). Analysis and Interpretation of Magnetotelluric Data in Characterization of Geothermal Resource in Eburru Geothermal Field, Kenya. *Geothermics, 81,* 12-31. https://doi.org/10.1016/j.geothermics.2019.04.003

Martí, A., Queralt, P., Ledo, J., & Farquharson, C. (2010). Dimensionality Imprint of Electrical Anisotropy in Magnetotelluric Responses. *Physics of the Earth and Planetary Interiors, 182,* 139-151. https://doi.org/10.1016/j.pepi.2010.07.007

McNeice, G. W., & Jones, A. G. (2001). Multisite, Multifrequency Tensor Decomposition of Magnetotelluric Data. *Geophysics, 66,* 158-173. https://doi.org/10.1190/1.1444891

Meqbel, N. M. M. (2009). *The Electrical Conductivity Structure of the Dead Sea Basin Derived from 2D and 3D Inversion of Magnetotelluric Data*. Doctoral Dissertation, Freie Universität Berlin.

Mibei, G. K. (2021). *The Magmatic Evolution, Eruptive History and Geothermal Reservoir Assessment of the Paka Volcanic Complex, Northern Kenya Rift*. PhD dissertation, University of Iceland, 200 pp. https://hdl.handle.net/20.500.11815/2706

Munoz, G. (2014). Exploring for Geothermal Resources with Electromagnetic Methods. *Surveys in Geophysics, 35,* 101-122. https://doi.org/10.1007/s10712-013-9236-0

Njue, L. M. (2014). Stratigraphic Model of Korosi Geothermal Prospect, Kenya. In *Proceedings of the 5th African Rift Geothermal Conference*.

Ochieng, L., Kipng'ok, J., Kanda, I., Igunza, G., & Wanjie, C. (2012). *Geochemistry of Fumarole Discharges and Borehole Waters of Korosi-Chepchuk Geothermal Prospect, Kenya*. The Geothermal Resources Council Transactions.

Omenda, P. A. (2010). The Geology and Geothermal Activity of the East African Rift. In *Proceedings of the Short Course VII on Exploration for Geothermal Resources*. UNU-GTP, GDC and KenGen.

Omollo, P., Nishijima, J., Fujimitsu, Y., & Sawayama, K. (2022). Resistivity Structural Imaging of the Olkaria Domes Geothermal Field in Kenya Using 2D and 3D MT Data Inversion. *Geothermics, 103,* Article 102414. https://doi.org/10.1016/j.geothermics.2022.102414

Parkinson, W. D. (1959). Directions of Rapid Geomagnetic Fluctuations. *Geophysical Journal International, 2,* 1-14. https://doi.org/10.1111/j.1365-246x.1959.tb05776.x

Revil, A., & Gresse, M. (2021). Induced Polarization as a Tool to Assess Alteration in Geothermal Systems: A Review. *Minerals, 11,* Article 962. https://doi.org/10.3390/min11090962

Savitri, K. P., Hecker, C., Deon, F., Sihotang, M. A., van der Meer, F. D., & Azis, H. (2022). The Link between Clay Composition and the Location of a Geothermal System Reservoir: A Case of Rantau Dedap Geothermal System. In *European Geothermal Congress 2022* (p. 179). European Geothermal Energy Council.

Simpson, F., & Bahr, K. (2005). *Practical Magnetotellurics*. Cambridge University Press. https://doi.org/10.1017/cbo9780511614095

Spichak, V., & Manzella, A. (2009). Electromagnetic Sounding of Geothermal Zones. *Journal of Applied Geophysics, 68,* 459-478. https://doi.org/10.1016/j.jappgeo.2008.05.007

Ussher, G., Harvey, C., Johnstone, R., Anderson, E., & Zealand, N. (2000). Understanding the Resistivities Observed in Geothermal Systems. In *Proceedings World Geothermal Congress* (pp. 1915-1920). Japanese Organizing Committee for WGC 2000 and the International Geothermal Association.

Van Leeuwen, W. A. (2016). *Geothermal Exploration Using the Magnetotelluric Method*. Doctoral Dissertation, Utrecht University.